Available online at www.sciencedirect.com
ScienceDirect
Journal of the European Ceramic Society 28 (2008) 1631–1639
www.elsevier.com/locate/jeurceramsoc

Laser ablation condensation and defect generation of $Ti_{1-x}Zr_xO_2$ nanoparticles

Meng-Hsiu Tsai [a], Pouyan Shen [a], Shuei-Yuan Chen [b,*]

[a] *Institute of Materials Science and Engineering, National Sun Yat-sen University Kaohsiung, Taiwan, ROC*
[b] *Department of Mechanical Engineering, I-Shou University Kaohsiung, Taiwan, ROC*

Received 7 June 2007; received in revised form 15 October 2007; accepted 26 October 2007
Available online 31 December 2007

Abstract

Defective dioxide nanocondensates of varied $Ti_{1-x}Zr_xO_2$ compositions and crystal structures, predominantly anatase, cubic (c-) and tetragonal (t-) fluorite type, were synthesized by energetic Nd-YAG laser pulse irradiation of the metal composite targets under oxygen background gas. The anatase-type was (0 0 1) faulted. The t-fluorite type $Ti_{1-x}Zr_xO_2$ has a larger size than the c-fluorite-type and tended to be {0 0 1} faulted due to partial transformation to monoclinic-symmetry. The nanocondensates formed dislocations, faults and twin via Brownian rotation–coalescence and/or relaxation of the joined particles.

Keywords: Laser ablation condensation; Electron microscopy; (Ti, Zr)O_2; Defects

1. Introduction

The motivation of this research is to synthesize $Ti_{1-x}Zr_xO_2$ solid solution nanoparticles with abundant defects and considerable residual stress by laser ablation condensation rather than relaxed nanoparticles by conventional sol–gel and then annealing route. $Ti_{1-x}Zr_xO_2$ solid solution and its defects are of concern to photocatalytic applications of Zr-dissolved anatase TiO_2.[1,2] Zr dopant has been used to stabilize TiO_2 as anatase structure at 1000 °C via hydrothermal solution route.[2] The inter-diffusion of Ti and Zr cations in fluorite-type structure is also interesting regarding to the concentration of charge- and/or volume-compensating oxygen vacancies and hence the stability of cubic (c-) and/or tetragonal (t-) structures in partially stabilized zirconia (PSZ).[3,4] (PSZ with various cation stabilizers has beneficial transformation toughening effect due to martensitic t- to monoclinic (m-) transformation.[5])

In our previous studies, pulse laser ablation with a very rapid heating/cooling and hence pressure effect has been used to fabricate fluorite-type dioxide nanocondensates of the end members of ZrO_2,[6–8] and TiO_2.[9] The t-ZrO_2 condensates were found to change shape yet with invariant plane strain as a result of t–m transformation under the influence of electron irradiation.[6] By contrast, the t-ZrO_2 condensates with considerable residual stress were allowed to relax or transform into c-phase upon electron dosage.[7,8] As for the fluorite-type TiO_2 condensates, they tended to transform martensitically to m- and then α-PbO_2-type structure following specific crystallographic relationships depending on the size of the condensates.[9] Defects were also found to generate for TiO_2 rutile particle via a coalescence process of the impinged nanocondensates.[10]

Here, pulse laser ablation was employed to fabricate $Ti_{1-x}Zr_xO_2$ nanocondensates focusing on the effect of such a dynamic process on the formation of dense Zr-doped titania and $Ti_{1-x}Zr_xO_2$ solid solution with c- and/or t-fluorite type structures partially underwent t–m transformation. Defect generation by the combined effects of dynamic solid solution, coalescence of the nanocondensates, and/or electron irradiation, was also addressed.

2. Experimental procedure

High purity (>99.2%) Zr and Ti foils 0.02 mm in thickness were used as target materials for energetic Nd-YAG-laser (Lotis, 1064 nm in wavelength, beam mode: TEM_{00}) pulse irradiation. The targets were satisfactory in producing $Ti_{1-x}Zr_xO_2$ conden-

* Corresponding author.
E-mail address: steven@isu.edu.tw (S.-Y. Chen).

0955-2219/$ – see front matter © 2007 Elsevier Ltd. All rights reserved.
doi:10.1016/j.jeurceramsoc.2007.10.008

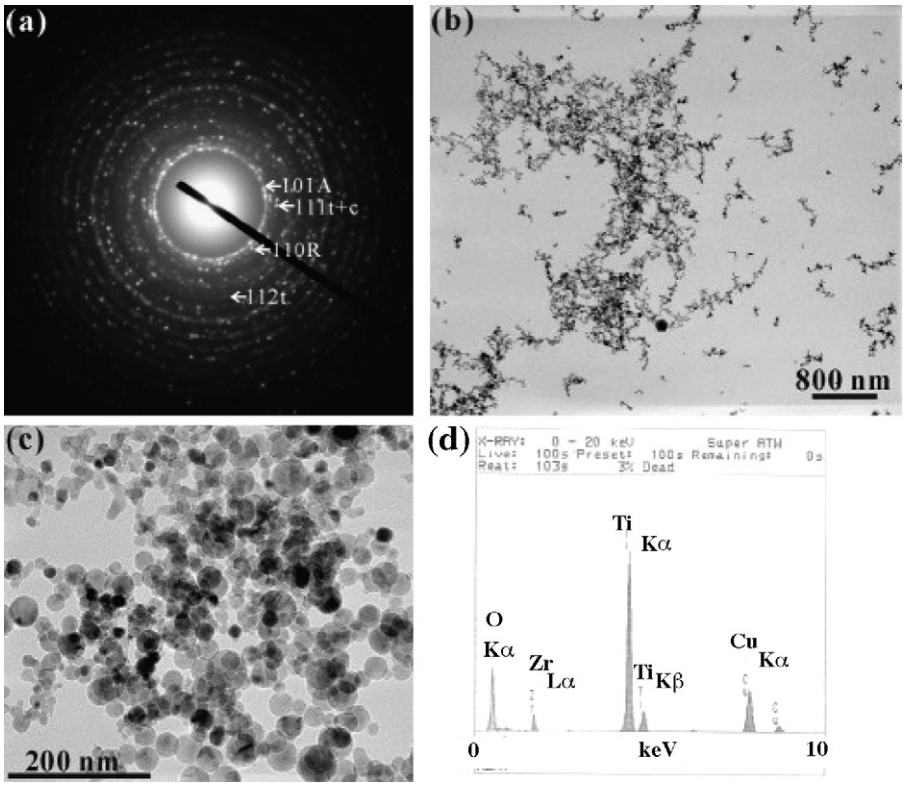

Fig. 1. TEM (a) SAED pattern and (b) and (c) BFIs at different magnifications showing the Ti-rich $Ti_{1-x}Zr_xO_2$ nanocondensates with anatase (denoted as A), rutile (denoted as R), t- and/or c-fluorite type structures were randomly oriented and assembled as NCA, (d) EDX spectrum showing predominant counts of Ti and O and minor counts of Zr with Cu peaks from supporting Cu ring. Specimen produced by laser ablation on the clamped Zr–Ti targets at 1.6×10^8 W/cm^2 and oxygen flow rate of 15 L/min.

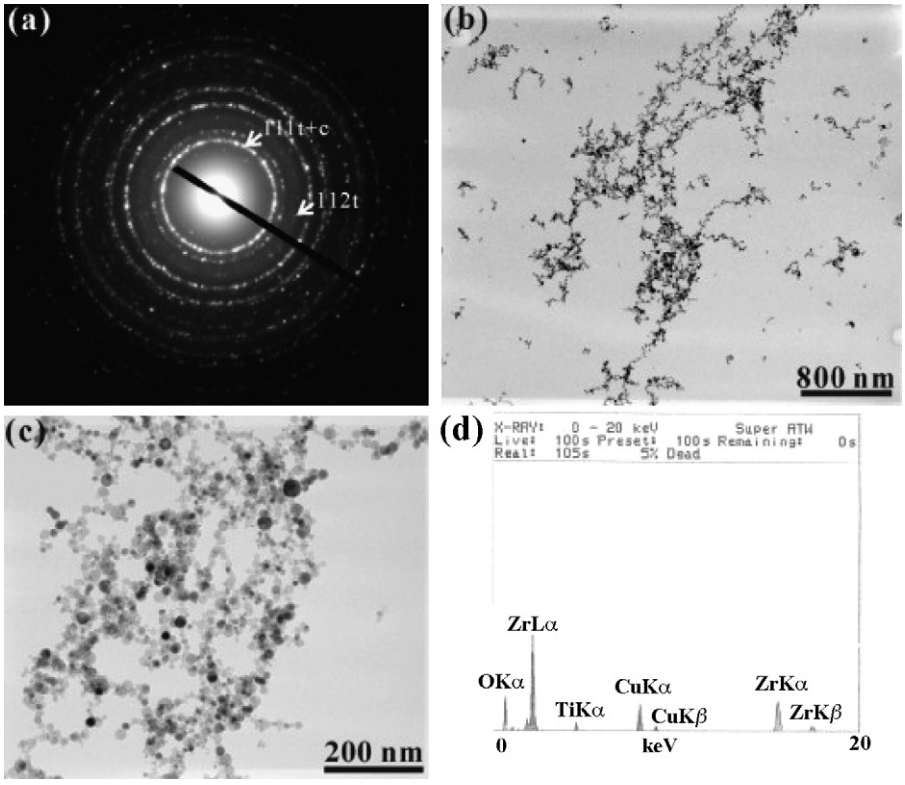

Fig. 2. TEM (a) SAED pattern and (b) and (c) BFIs at different magnifications showing the Zr-rich $Ti_{1-x}Zr_xO_2$ nanocondensates with t- and/or c-fluorite type structures were randomly oriented and assembled as NCA, (d) EDX spectrum showing predominant counts of Zr and O and minor counts of Ti with Cu peaks from supporting Cu ring. Specimen produced by laser ablation on the clamped Zr-Ti targets at 1.6×10^8 W/cm^2 and oxygen flow rate of 15 L/min

sates without detectable impurities. The Lotis laser pulse time duration was 240 μs at 10 Hz, having the laser beam focused to a spot area of 0.03 mm^2 on the clamped Zr–Ti (i.e. Zr on the laser incident side) or Ti–Zr (i.e. Ti on the laser incident side) targets inside the ablation chamber. Oxygen (99.999% purity) was supplied near a fixed flow rate of 5, 15, 20 and 25 L/min to oxidize, condense and cool the metal vapor. A laser input energy of 1150 and 635 mJ/pulse, i.e. power density of 1.6×10^8 and 8.8×10^7 W/cm^2, respectively under the mentioned pulse time duration, frequency and spot size, assured a good yield of $Ti_{1-x}Zr_xO_2$ condensates. (The rate of nanoparticles formation depends on the target ablation rate. In general, more than 10^{12} nanoparticles were produced within minutes of the present pulsed laser ablation process indicating it can be an alternative fabrication route in the future.)

Copper grids overlaid with a carbon-coated collodion film and fixed in position by a plastic holder at a distance of 2.5–10 mm from the composite targets were used to collect the condensates. The composition and crystal structures of the $Ti_{1-x}Zr_xO_2$ condensates were characterized by analytical electron microscopy (AEM, JEOL 3010 instrument at 300 keV) with selected area electron diffraction (SAED), and point-count energy dispersive X-ray (EDX) analysis at a beam size of 10 nm. Scanning transmission electron microscopy (STEM) (FEI Tecnai G2F20 at 200 kV) coupled with EDX analysis was also used to analyze detailed composition of the particles. Bright field images (BFI) taken by transmission electron microscopy (TEM) were used to study the general morphology and agglomeration of the condensed $Ti_{1-x}Zr_xO_2$ particles. Lattice imaging coupled with two-dimensional Fourier transform and inverse transform were used to analyze the crystal structure of nano-size particles and their phase transformation, if any, upon electron irradiation. The t-fluorite type $Ti_{1-x}Zr_xO_2$ was indexed according to the distorted version of c-fluorite type parent cell. The d-spacings measured from SAED patterns were used for least-squares refinement of the lattice parameters.

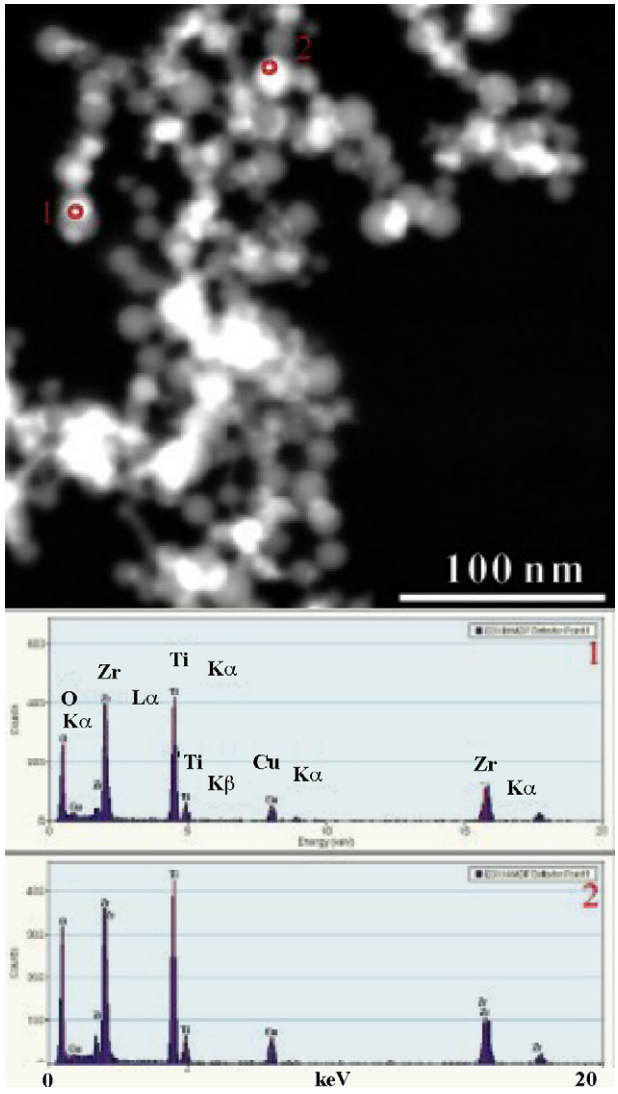

Fig. 3. STEM-EDX spectra of two individual $Ti_{1-x}Zr_xO_2$ nanocondensates with different chemical composition. Specimen produced by laser ablation on the clamped Zr–Ti targets at 8.8×10^7 W/cm^2 and oxygen flow rate of 25 L/min.

3. Results

The laser ablation condensation products are aggregates of nanometer-size and randomly oriented $Ti_{1-x}Zr_xO_2$ dioxide particles, i.e. Zr-doped anatase and rutile, and cubic (c-) and/or tetragonal (t-) fluorite type structures, regardless of the adopted laser power density, the target sequence of Zr–Ti or Ti–Zr, and the oxygen flow rates from 5 to 25 L/min. Anatase appeared to be a predominant titania phase in the presence of Zr dopant in accord with previous observations of samples prepared by hydrothermal and then annealing route.[2] The typical microstructures, composition and phase identification results of the predominant phases are as follows.

TEM BFI (Figs. 1b and 2b) indicated the $Ti_{1-x}Zr_xO_2$ nanoparticles were assembled as nano-chain aggregates (NCA) or in close packed manner, regardless of composition variation. Electron diffraction (Figs. 1a and 2a) and EDX spectra further indicated the predominant nanocondensates are Zr-doped anatase in Ti-rich region (Fig. 1c and 1d) whereas t- and/or c-fluorite type structures in Zr-rich region (Fig. 2c and 2d). In fact, the composition varied from particle to particle (Fig. 3) according to STEM-EDX analysis on individual nanoparticles using a beam size of 10 nm.

The Zr-doped anatase has faults parallel to (0 0 1) and dislocation half plane parallel to (0 $\bar{1}$ 1) and (0 0 1) as indicated by the lattice image (Fig. 4a), two-dimensional Fourier transform (Fig. 4b) and inverse transform (Fig. 4c) of the condensate with a relatively large diameter of 30 nm. By contrast, the Zr-doped anatase condensate with a smaller diameter of 15 nm was found to be nearly dislocation free (Fig. 5).

As for the $Ti_{1-x}Zr_xO_2$ condensate with t-fluorite type structure, it has commensurate faults parallel to the (0 0 1) plane and hence (0 0 1) spot as shown by its lattice image (Fig. 6a), two-dimensional Fourier transform (Fig. 6b) and inverse transform (Fig. 6c). Such t-fluorite type nanocondensates with a relatively large diameter of ~25 nm (Fig. 7) was partially transformed to monoclinic (m-) symmetry with the t/m interface and the fault plane of m-phase parallel to (0 0 1).

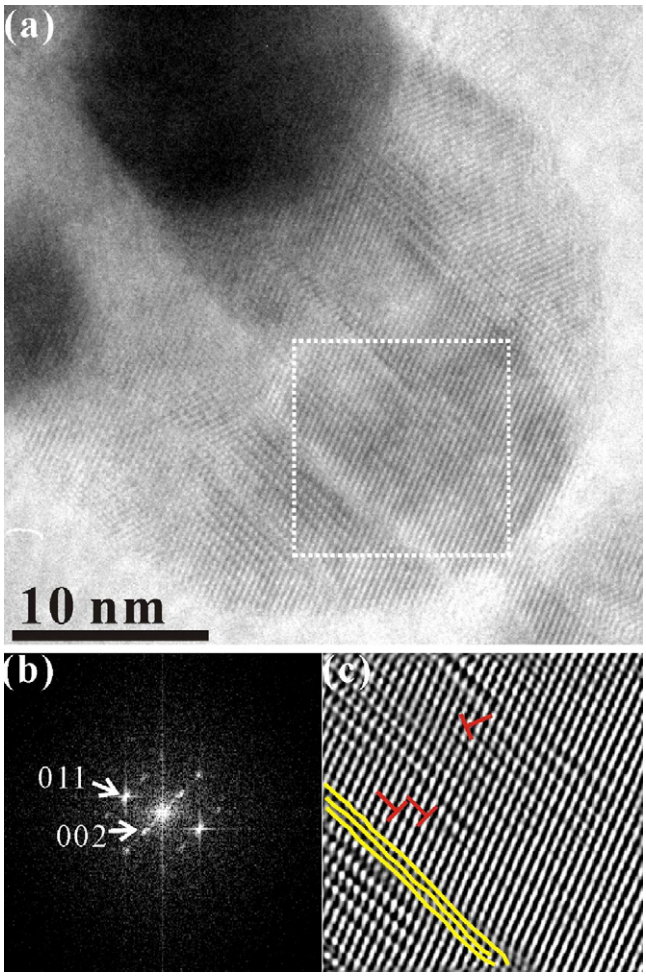

Fig. 4. (a) Lattice image and (b) two-dimensional Fourier transform along with (c) inverse transform showing a Zr-doped anatase condensate about 30 nm in diameter has faults parallel to (0 0 1) and dislocation half plane parallel to (0 $\bar{1}$ 1) and (0 0 1). The same specimen as in Fig. 1.

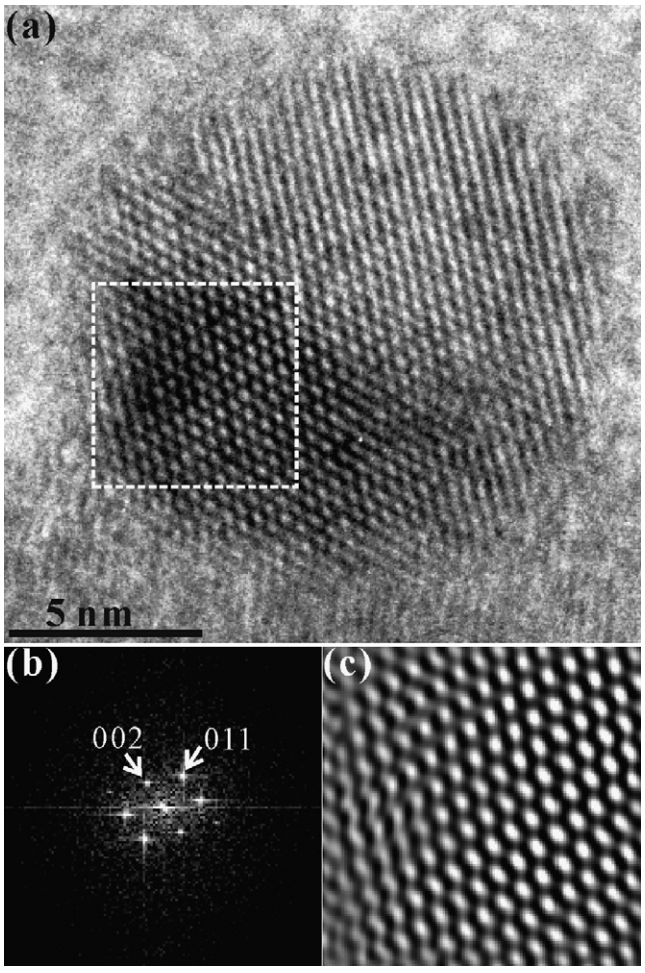

Fig. 5. (a) Lattice image and (b) two-dimensional Fourier transform along with (c) inverse transform showing a Zr-doped anatase condensate about 15 nm in diameter is defect free. The same specimen as in Fig. 1.

The $Ti_{1-x}Zr_xO_2$ nanocondensates with c-fluorite type structure have well-developed {1 1 1} and {1 0 0} facets and are free of dislocations when small in size (~10 nm) (Fig. 8). However, two such c-fluorite type nanoparticles were found to coalesce and/or relax to form twinned bicrystals following {1 1 1} twin plane and domain boundary {0 1 1} {1 1 1}, as manifested by the impinged corner in Fig. 9. Alternatively, c-fluorite type nanoparticles were coalesced into unity with interfacial dislocations having half plane parallel to (1 0 0) and (1 $\bar{1}$ 1) (Fig. 10). The dislocations were predominantly generated in the impinged corner, especially near the interface of the smaller particle in the lower right hand side corner of the figure. The defects were introduced by a rotation–coalescence event of the impinged $Ti_{1-x}Zr_xO_2$ nanoparticles as discussed later.

4. Discussion

4.1. Polyhedral site and lattice mismatch upon mutual dissolution of TiO_2 and ZrO_2

The fluorite-related related $Ti_{1-x}Zr_xO_2$ nanocondensates have a wide composition range, whereas the anatase and rutile type are Ti-rich. The mutual dissolution of the end members at the scale of individual particles predominantly occurred during the dynamic ablation–condensation process, although interdiffusion to approach the solid solution limit at ambient pressure[11] could happen between the coalesced particles. The mutual dissolution of the components as well as the residual stress would affect the lattice parameters, as addressed in the following.

The least-squares refinement of the d-spacings of the present condensates indicated that the dissolution of larger-size Zr cation caused negligible change of room-temperature lattice parameters for rutile ($a = 0.459$ nm and $c = 0.296$ nm) and anatase ($a = 0.379$ nm and $c = 0.951$ nm) in comparison with the undoped rutile ($a = 0.4593$ nm and $c = 0.2959$ nm, JCPDS file 21-1276) and anatase ($a = 0.3785$ nm and $c = 0.9513$ nm, JCPDS file 21-1272). This may be accounted for by the residual compressive stress imposed by the ablation–condensation process. (Pressure effect due to rapid heating/cooling in a dynamic laser ablation condensation process was suggested for the retention of dense TiO_2 condensate of α-PbO_2-type structure and fluorite-type related structure[9,12] as well as the t-ZrO_2 condensates.[7,8]) On the other hand, Ti-dissolution caused significantly smaller cell parameter for the c-ZrO_2 condensates ($a = 0.509$ nm) than

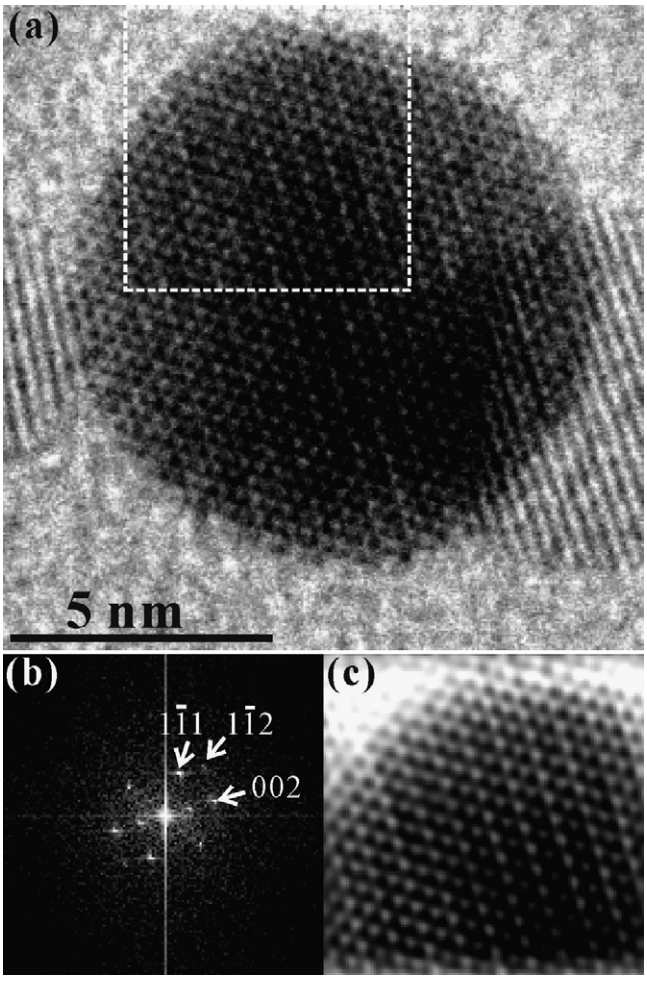

Fig. 6. (a) Lattice image and (b) two-dimensional Fourier transform along with (c) inverse transform showing the t-fluorite type condensate has commensurate fault along (0 0 1) plane and hence (0 0 1) diffraction spot. The same specimen as in Fig. 1.

pure c-ZrO_2 ($a = 0.5128$ nm, JCPDS file 49-1642). A smaller cell volume for Ti-dissolved zirconia than the undoped case is due to the replacement of Zr^{4+} (0.084 nm) by smaller Ti^{4+} (0.074 nm) in coordination number (CN) 8 given the effective radii of cations,[13] besides a possible effect of residual compressive stress.

The polyhedral site and/or lattice mismatch are of concern to dislocation generation and migration to the free surface. The mutual dissolution of the TiO_2 and ZrO_2 component caused a mismatch by more than 15% at substitution site for all the condensates. The overall change of the cell volume due to mutual dissolution is however one order of magnitude smaller that that at individual polyhedral sites. For example, the Ti-dissolved c-ZrO_2 condensates suffered 0.74% decrease in d-spacings comparing to the undoped c-ZrO_2. Shear stress up to ca. 0.5 ± 0.1 and 1.3 ± 0.1 GPa are therefore built up for the $\{1\,0\,0\}$ and $\{1\,1\,0\}$ planes, respectively, given the shear moduli c and c′ for analogue oxide with fluorite-type isostructure. (The shear moduli c and c′ correspond to shear on the $\{1\,0\,0\}$ and $\{1\,1\,0\}$ planes in a cubic system, respectively,[14] where $c = C_{44} = 56$ GPa and $c' = 1/2\,(C_{11}–C_{22}) = 153$ GPa for analogue cubic ZrO_2 with

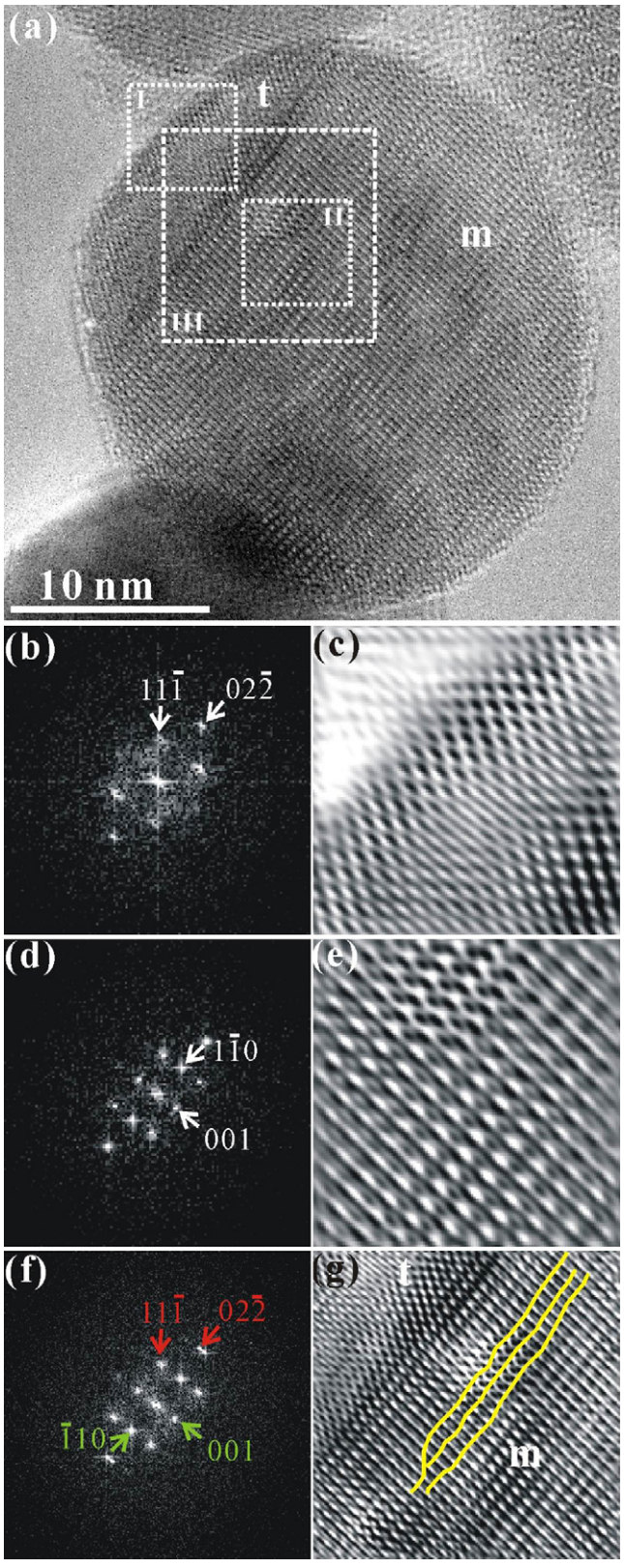

Fig. 7. (a) Lattice image and (b) two-dimensional Fourier transform along with (c) inverse transform showing the t-fluorite type nanocondensates about 25 nm in diameter was partially transformed to m-symmetry with the t/m interface and fault plane parallel to (0 0 1). Specimen produced by laser ablation on the clamped Zr–Ti targets at 1.6×10^8 W/cm^2 and oxygen flow rate of 25 L/min.

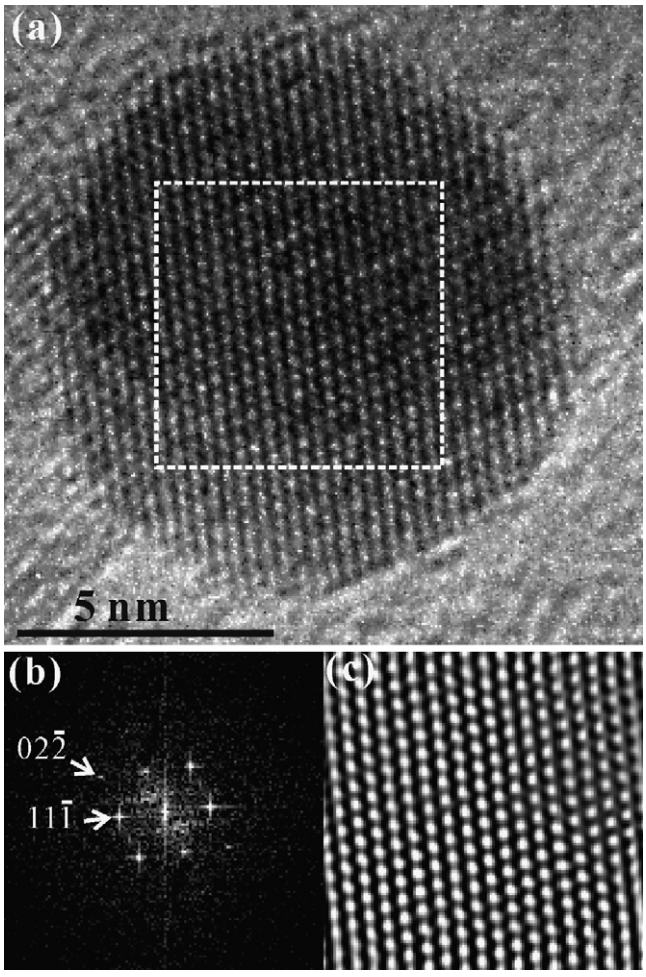

Fig. 8. (a) Lattice image and (b) two-dimensional Fourier transform along with (c) inverse transform showing the c-fluorite type nanocondensate about 10 nm in diameter has well-developed {1 1 1} and {1 0 0} facets and free of dislocation. The same specimen as in Fig. 7.

8 mol% Y_2O_3.[15]) Such stress levels are equal to or even more than that required (~0.5 GPa) to activate slip system for fluorite-type oxides.[16,17]

4.2. Chemical stabilization of c- and t-fluorite type structures

Compressive stress due to rapid heating-cooling of a laser ablation process under the influence of oxygen background gas was suggested to stabilize the TiO_2,[9] and ZrO_2 condensates[7,8] as c-fluorite type structure. The possible residual stress of the present $Ti_{1-x}Zr_xO_2$ nanocondensates is difficult, if not impossible, to determine due to overwhelming chemical effect.

The c-fluorite type structure could be alternatively stabilized by mutual dissolution of TiO_2 and ZrO_2 upon dynamic laser ablation condensation under oxygen flow or electron irradiation in vacuum. Tramp impurities of Ti^{2+} and/or Ti^{3+}, if incorporated in such processes, would substitute for Zr^{4+} in CN 8 and hence introduce charge-compensating oxygen vacancies to stabilize the c-fluorite structure. The stabilization of c-ZrO_2 resulting from oxygen vacancies was supported by experimental evi-

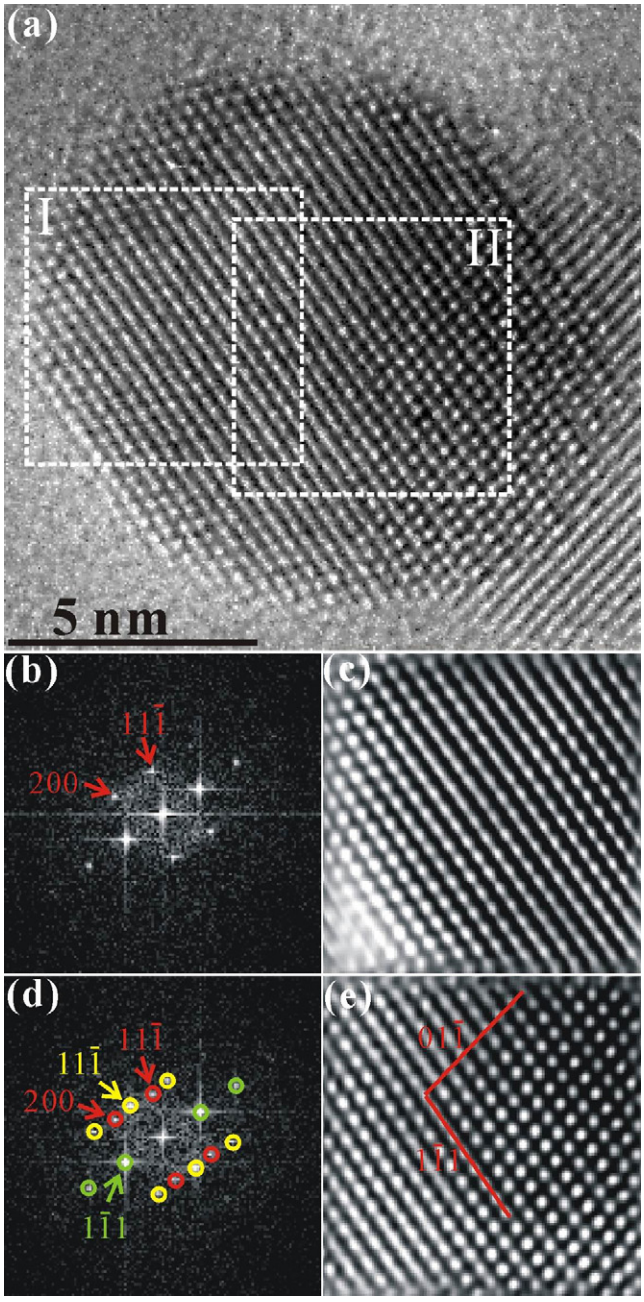

Fig. 9. (a) Lattice image and (b) two-dimensional Fourier transform along with (c) inverse transform showing two c-fluorite type nanoparticles about 10 nm in size were coalesced and/or relaxed to form twinned bicrystals. The same specimen as in Fig. 7.

dences on the Zr–ZrO_2 system[18] and the annealed thin zirconia film.[19] Theoretical calculations using a self-consistent tight-binding model also indicated that the large relaxation around an oxygen vacancy, and the clustering of vacancies along the ⟨1 1 1⟩ directions are in good agreement with experiments and first principles calculations.[20]

As for t-fluorite type structure, various explanations have been proposed for the observed stabilization of high temperature t-phase in nanocrystalline zirconia particles at room temperature and controversies still exist in the elucidation of the mechanism of t-phase stability. Osendi et al.[21] postulated that the

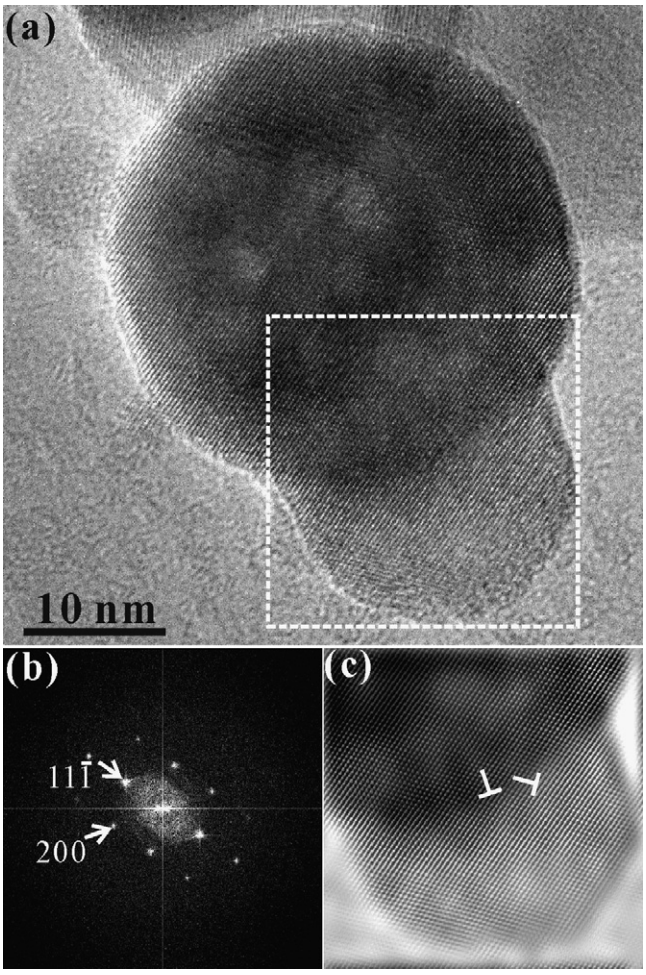

Fig. 10. (a) Lattice image and (b) two-dimensional Fourier transform along with (c) inverse transform showing two c-fluorite type nanoparticles about 20 nm in size were coalesced as a single crystal with dislocations (half plane parallel to (1 0 0) and (1 $\bar{1}$ 1)) near the interface of the smaller particle in the lower right hand side corner. Specimen produced by laser ablation on the clamped Ti–Zr targets at 1.6×10^8 W/cm^2 and oxygen flow rate of 20 L/min.

initial nucleation of t-ZrO_2 is favored by anionic vacancies with trapped electrons. Tani et al.[22] proposed a mechanism of topotactic crystallization of t-ZrO_2 on nuclei in the amorphous ZrO_2. The oxygen purging and $Ti_{1-x}Zr_xO_2$ solid solution in the present laser ablation condensation process may suppress oxygen vacancies in local area to favor t- rather than c-fluorite type structure. In any case, kinetically, the former can transform to later and vice versa depending on the intersection of the free energy versus composition curve[23] and/or the free energy versus cell volume curve when the extent of residual stress is of concern.[7,8] (Dense t-ZrO_2 nanocondensates with a residual stress above 6 GPa was found to transform into a metastable cubic phase due to size-dependent free energy vs. volume curves for the c- and t-polymorphs at specific temperature in pure ZrO_2 system.[7,8]) For ZrO_2–TiO_2 binary, additional chemical free energy effect needs to be considered for the construction of isothermal free energy envelopes as a function of both volume and composition, which is beyond the scope of the present study.

4.3. Martensitic transformation of nanosize t-fluorite type $Ti_{1-x}Zr_xO_2$ particles

Defect-facilitated nucleation has been suggested for the transformation of small ZrO_2 particles embedded in metal and ceramics matrices. For t-ZrO_2 particles in Cu matrix and HfO_2 particles in Ta matrix, the martensitic nucleation was often suppressed by the lack of potent defects.[24,25] When such defects are available, nucleation of m-phase occurred spontaneously in the internal stress field of the nucleating defects. Abundant point defects and the free surface of the present $Ti_{1-x}Zr_xO_2$ condensates would also act as nucleation sites for t–m transformation.

The t-fluorite type $Ti_{1-x}Zr_xO_2$ partially transformed to m-symmetry upon electron irradiation showed (0 0 1) habit plane and fault plane. Analogously the undoped t-ZrO_2 nanocondensates transformed to m-symmetry forming {1 0 0} and {1 1 0} twin plane with resultant shape and volume changes under the influence of electron-irradiation and thermal stress.[6] The m-twinning plane, either induced by cooling or under the influence of an applied stress, was however reported to be on (1 0 0), (0 0 1), and (1 1 0) for pure ZrO_2 and a number of PSZ and zirconia-dispersed ceramics exhibiting mosaic twins and closure twins.[5] In any case, the individual t-fluorite type $Ti_{1-x}Zr_xO_2$ condensates are expected to have beneficial transformation toughening effect due to martensitic t–m transformation analogous to tetragonal zirconia polycrystals.[5]

4.4. Brownian rotation and defect generation of the coalesced nanocondensates

The ($h\,k\,l$) surface specific coalescence has been shown to occur for laser ablation produced nanocondensates of CeO_2,[26] t-ZrO_2,[6] TiO_2 rutile[10] and nonstoichiometric CeO_{2-x}.[27] When such nanocondensates were imperfectly attached as expected to be the case in general, Brownian rotation of the particles above a critical temperature for anchorage release at interface is required as for the case of f.c.c. metal crystallites migrating and rotating on single crystal substrate, KCl(1 0 0) with or without steps (Appendix).[28–33]

Besides {$h\,k\,l$}-specific coalescence, some $Ti_{1-x}Zr_xO_2$ nanocondensates with poorly developed facets tended to coalesce via arbitrarily impinged corner, which can be rationalized by so-called grain rotation coalescence.[34] In such model, the two neighboring grains would finally assume the same orientation[34] because of grain boundary anisotropy.[33] In fact, anisotropic grain boundary energy depends on the misorientation angle between any two neighboring grains,[35] and the change of the orientation of one grain due to rotation leads to a change in the misorientations of all the grain boundaries surrounding the grain change such that overall the total energy of all grain boundaries delimiting the grain decrease.

Finally, sintering stress associated with the impinged corner would account for the dislocation generation, whereas {$h\,k\,l$}-specific coalescence would explain faults and twin for the $Ti_{1-x}Zr_xO_2$ condensates analogous to the condensates of TiO_2 rutile[10] and SnO_2 rutile.[36] In fact, stress relaxation was found to

cause a high density of fault and dislocation near the coalescence twin plane for the condensate of TiO_2 rutile.[10]

5. Conclusions

1. Laser ablation on Zr–Ti or Ti–Zr target at a high power density of 8.8×10^7 or 1.6×10^8 W/cm^2 and varied oxygen flow rates from 5 to 25 L/min produced nanometer-size and randomly oriented $Ti_{1-x}Zr_xO_2$ solid solution particles with predominant anatase and fluorite type of c- and t-structures.
2. The Zr-doped anatase was (0 0 1) faulted whereas the t-fluorite type $Ti_{1-x}Zr_xO_2$ with a larger size than the c-fluorite-type was {0 0 1} faulted and partially transformed to m-symmetry.
3. The $Ti_{1-x}Zr_xO_2$ nanocondensates were coalesced via an arbitrary impinged corner or specific low-index contact plane followed by a Brownian rotation process in order to be unified or twinned.
4. Point defects were introduced by mutual solid solution, whereas dislocations and planar defects, i.e. fault and twin plane, via the coalescence and/or martensitic transformation of the $Ti_{1-x}Zr_xO_2$ condensates.

Acknowledgments

We thank L.J. Wang for technical assistance on STEM and the anonymous referee for constructive comments. Supported by Center for Nanoscience and Nanotechnology at NSYSU and National Science Council, Taiwan, ROC under contract NSC94-2120-M110-001.

Appendix A. Brownian rotation–coalescence of crystallites on single crystal substrate

Experimentally, f.c.c. metal crystallites have been proved to be able to migrate-rotate[28] and coalesce[29] on the free surface of single crystal substrate regardless of the presence of surface steps[30] until low-energy epitaxial orientation with respect to the substrate was reached. (Refer to Kuo and Shen[31] for the retrospect of the experimental results and theoretical considerations of Brownian-type rotation of non-epitaxial crystallites on single crystal substrate.) Einstein's molecular theory of heat, Eyring's transition state model and frictional force at a viscous interface were successfully adopted to formulate the diffusivity equation of the crystallite over the single crystal substrate.[29,32] A critical temperature (T_c) must be reached for anchorage release and for the crystallites to move under a frictional force related to interfacial viscosity. In general, T_c is lower for smaller particle size, and nanometer-size Au particles have been proved to migrate-rotate and coalesce on KCl(1 0 0) substrate at 94 °C.[28] More recent annealing of the ⟨1 1 1⟩ textured films of gold prepared by thermal evaporation indicated that the individual grains constantly rotate about the film normal.[33] It was suggested that each grain was free to rotate about an axis perpendicular to the plane in the clockwise or counterclockwise direction.

References

1. Yu, J. C., Lin, J. and Kwok, R. W. M., $Ti_{1-x}Zr_xO_2$ solid solution for photocatalytic degradation of acetone in air. *J. Phys. Chem. B*, 1998, **102**, 5094–5098.
2. Hirano, M., Nakahara, C., Ota, K., Tanaike, O. and Inagaki, M., Photoactivity and phase stability of ZrO_2-doped anatase-type TiO_2 directly formed as nanometer-sized particles by hydrolysis under hydrothermal conditions. *J. Solid State Chem.*, 2003, **170**, 39–47.
3. Lin, C. L., Gan, D. and Shen, P., Stabilization of ZrO_2 sintered with Ti. *J. Am. Ceram. Soc.*, 1988, **71**(8), 624–629.
4. Lin, C. L., Gan, D. and Shen, P., The effects of TiO_2 addition on the microstructure and transformation of ZrO_2 with 3 and 6 mol% Y_2O_3. *Mater. Sci. Eng. A*, 1990, **129**, 147–155.
5. Green, D. J., Hannink, R. H. J. and Swain, M. V., *Transformation Toughening of Ceramics*. CRC Press, Boca Raton, FL, 1989, pp. 1–232.
6. Shen, P. and Lee, W. H., (1 1 1)-specific coalescence twinning and martensitic transformation of tetragonal ZrO_2 condensates. *Nano Lett.*, 2001, **1**, 707–711.
7. Tsai, M. H., Chen, S. Y. and Shen, P., Condensation and relaxation/transformation of dense t-ZrO_2 nanoparticles. *J. Chem. Phys.*, 2005, **122**, 204708-1–6.
8. Tsai, M. H., Chen, S. Y. and Shen, P., Laser ablation condensation of polymorphic ZrO_2 nanoparticles: effects of laser parameters, residual stress and kinetic phase change. *J. Appl. Phys.*, 2006, **99**, 054302-1–8.
9. Chen, S. Y. and Shen, P., Laser ablation condensation and transformation of baddeleyite-type related TiO_2. *Jpn. J. Appl. Phys.*, 2004, **43**, 1519–1524.
10. Tsai, M. H., Chen, S. Y. and Shen, P., Imperfect orientated attachment: accretion and defect generation of nanosize rutile condensates. *Nano Lett.*, 2004, **4**, 1197–1201.
11. McHale, A. E. and Roth, R. S., Low-temperature phase relationships in the system ZrO_2–TiO_2. *J. Am. Ceram. Soc.*, 1986, **69**(11), 827–832.
12. Chen, S. Y. and Shen, P., Laser ablation condensation of α-PbO_2-type TiO_2. *Phys. Rev. Lett.*, 2002, **89**, 096106-1–4.
13. Shannon, R. D., Revised effective ionic radii and systematic studies of interatomic distances in halides and chalcogenides. *Acta Crystallogr. A*, 1976, **32**, 751–767.
14. Poirier, J. P., *Introduction to the Physics of the Earth's Interior*. Cambridge University Press, Cambridge, 1991, p. 15.
15. Kandil, H. M., Greiner, J. D. and Smith, J. F., Single-crystal elastic constants of yttria-stabilized zirconia in the range 20 to 700 °C. *J. Am. Ceram. Soc.*, 1984, **67**, 341–346.
16. Evan, A. G. and Pratt, P. L., Dislocation in the fluorite structure. *Philos. Mag.*, 1969, **20**, 1213–1236.
17. Fries, E., Guiberteau, F., Dominguez-Rodrigue, A., Cheong, D. S. and Heuer, A. H., High-temperature plastic deformation of Y_2O_3-stabilized ZrO_2 single crystals. I. The origin of the yield drop and associated glide polygonization. *Philos. Mag. A*, 1989, **60**, 107–121.
18. Ruh, R. and Garrett, H. J., Nonstoichiometry of ZrO_2 and its relation to tetragonal-cubic inversion in ZrO_2. *J. Am. Ceram. Soc.*, 1967, **50**, 257–261.
19. El-Shanshoury, I. A., Rudenko, V. A. and Ibrahim, I. A., Polymorphic behavior of thin evaporated films of zirconium and hafnium oxides. *J. Am. Ceram. Soc.*, 1970, **53**, 264–268.
20. Fabris, S., Paxton, A. T. and Finnis, M. W., A stabilization mechanism of zirconia based on oxygen vacancies only. *Acta Mater.*, 2002, **50**, 5171–5178.
21. Osendi, M. I., Moya, J. S., Serna, C. J. and Soria, J., Metastability of tetragonal zirconia powders. *J. Am. Ceram. Soc.*, 1985, **68**, 135–139.
22. Tani, E., Yoshimura, M. and Somiya, S., Formation of ultrafine tetragonal ZrO_2 powder under hydrothermal conditions. *J. Am. Ceram. Soc.*, 1985, **66**, 11–14.
23. Chen, S. and Shen, P., Polymorphic transformation of t′-phase in yttria partially stabilized zirconia. *Mater. Sci. Eng. A*, 1990, **123**, 145–152.
24. Chen, I. W. and Chiao, Y. H., Martensitic nucleation in ZrO_2. *Acta Metall.*, 1983, **31**, 1627–1638.
25. Chen, I. W. and Chiao, Y. H., *In Science and Technology of Zirconia in Advances in Ceramics*, *12*, ed. A. H. Heuer and L. W. Hobbs. American Ceramics Society, Columbus, OH, 1984, p. 33.

26. Kuo, L. Y. and Shen, P., Shape dependent coalescence and preferred orientation of CeO_2 nanocrystallites. *Mater. Sci. Eng. A*, 2000, **227**, 258–265.
27. Lee, W. H. and Shen, P., Laser ablation deposition of CeO_{2-x} epitaxial domains on glass. *J. Solid State Chem.*, 2002, **166**, 197–202.
28. Masson, A., Métois, J. J. and Kern, R., Migration brownienne de crystallites surune surface et relation avec l'épitaxie I. Partie expérimentale. *Surf. Sci.*, 1971, **27**, 463–482.
29. Métois, J. J., Gauch, M., Masson, A. and Kern, R., Migration brownienne de cristallites sur une surface et relation avec l'épitaxie. III. Cas de l'aluminium sur KCl: Précisions sur le méchanisme de glissement. *Surf. Sci.*, 1972, **30**, 43–52.
30. Métois, J. J., Migration brownienne de cristallites sur une surface et relation avec l'épitaxie. IV. Mobilité de crystallites sur une surface: Décoration de gradins monoatomiques de surface. *Surf. Sci.*, 1973, **36**, 269–280.
31. Kuo, L. Y. and Shen, P., On the rotation of non-epitaxy crystallites on single crystal substrate. *Surf. Sci.*, 1997, **373**, L350–L356.
32. Kern, R., Masson, A. and Métois, J. J., Migration brownienne de crystallites surune surface et relation avec l'épitaxie. II. Partie théorique. *Surf. Sci.*, 1971, **27**, 483–498.
33. Harris, K. E., Singh, V. V. and King, A. H., Grain rotation in the thin films of gold. *Acta Mater.*, 1998, **46**, 2623–2633.
34. Moldovan, D., Yamakov, V., Wolf, D. and Phillpot, S. R., Scaling behavior of grain-rotation induce grain growth. *Phys. Rev. Lett.*, 2002, **89**, 206101-1 to 4.
35. Humphreys, J. F. and Hatherly, M., *Recrystallization and Related Annealing Phenomena*. Pergamon, 1995.
36. Tseng, W. J., Shen, P. and Chen, S. Y., Defect generation of rutile-type SnO_2 nanocondensates: imperfect oriented attachment and phase transformation. *J. Solid State Chem.*, 2006, **179**, 1237–1246.